

Fall Technical Meeting
of the Western States Section of the Combustion Institute
Hosted by the University of California, Irvine, CA
Oct 26-27, 2009

A High-Order Projection Scheme for AMR Computations of Chemically Reacting Flow

C. Safta, J. Ray, H.N. Najm

Sandia National Laboratories, Livermore, CA 94551-0969, USA

A high-order projection scheme was developed for the study of chemically reacting flows in the low-Mach number limit. The numerical approach for the momentum transport uses a combination of cell-centered/cell-averaged discretizations to achieve a fourth-order formulation for the pressure projection algorithm. This scheme is coupled with a second-order in time operator-split stiff approach for the species and energy equations. The code employs a fourth-order, block-structured, adaptive mesh refinement approach to address the challenges posed by the large spectrum of spatial scales encountered in reacting flow computations. Results for 1D and 2D laminar flame configurations are used to illustrate the performance of the numerical construction.

Introduction

Since the detailed structure and various non-equilibrium characteristics of chemical reacting systems are difficult and costly to obtain experimentally, numerical simulation is an important tool in complementing experimental investigations of combustion processes. Chemical reacting systems based on hydrocarbon fuels typically exhibit a large spectrum of characteristic spatial and temporal scales. The complexity of kinetic models even for simple hydrocarbon fuels compounds this problem making multidimensional numerical simulations difficult even for laboratory scale configurations.

These difficulties are commonly addressed in a variety of ways. For low speed flows, one may adopt a low Mach number approximation [1] for the momentum transport. This approximation assumes that acoustic waves travel at infinite speed, a justifiable assumption in many low-speed flows. One can also exploit the structure of the governing equations and adopt an operator-split mechanism, performing the transport and reactive time-advancement via specialized integrators [2]. In problems where fine structures exist only in a small fraction of the domain e.g. in laminar jet flames, one may employ adaptive mesh refinement (AMR) [3] to concentrate resolution only where needed [4–7], while maintaining a coarse mesh resolution elsewhere.

We have recently developed a numerical model that aims to address some of the challenges posed by the use of AMR for reacting flow computations. In order to reduce the number of grid points and the number of refinement levels in the computational mesh hierarchy we employ high-order stencils to discretize the transport equations and to interpolate between the computational blocks on adjacent mesh levels. A projection scheme is employed

for the momentum transport. Since in most reacting flows mesh adaptivity is driven by the narrow flame structure rather than the velocity field, we are solving the momentum transport on a uniform mesh only. This further enhances the efficiency of the model since the elliptic solver required by the pressure equation is more efficient on a uniform mesh compared to a multilevel one [8]. The numerical approach and results obtained for canonical configurations are presented below.

Computational Model

In the low-Mach number limit, the continuity, momentum and scalar transport equations for a chemically reacting system are written in compact form as

$$\nabla \cdot \mathbf{v} = -\frac{1}{\rho} \frac{D\rho}{Dt} \quad (1a)$$

$$\frac{\partial \mathbf{v}}{\partial t} = -\frac{1}{\rho} \nabla p + C_U + D_U \quad (1b)$$

$$\frac{\partial T}{\partial t} = C_T + D_T + S_T \quad (1c)$$

$$\frac{\partial Y_k}{\partial t} = C_{Y_k} + D_{Y_k} + S_{Y_k} \quad k = 1, 2, \dots, N_s \quad (1d)$$

Here \mathbf{v} is the velocity vector, ρ the density, T the temperature, Y_k the mass fraction of species k , p is the hydrodynamic pressure, and N_s is the number of chemical species. The $\frac{D}{Dt}$ operator in the continuity equation represents the material derivative, $\frac{D}{Dt} = \frac{\partial}{\partial t} + \mathbf{v} \cdot \nabla$. The system of transport equations is closed with the equation of state for an ideal gas:

$$P_0 = \frac{\rho \mathfrak{R} T}{\bar{W}} = \rho \mathfrak{R} T \sum_{k=1}^{N_s} \frac{Y_k}{W_k} = \text{const} \quad (2)$$

where P_0 is the thermodynamic pressure, \mathfrak{R} is the universal gas constant, W_k is the molecular weight of species k , and \bar{W} is the molecular weight of the mixture. The thermodynamic pressure is constant in time and spatially uniform for an open domain in the low-Mach number limit.

The convection and diffusion terms in (1) are given by

$$C_U = -(\mathbf{v} \cdot \nabla) \mathbf{v}, \quad D_U = \frac{1}{\rho} \nabla \cdot \boldsymbol{\tau}, \quad (3a)$$

$$C_T = -(\mathbf{v} \cdot \nabla) T, \quad D_T = \frac{1}{\rho c_p} \nabla \cdot (\lambda \nabla T) - \frac{1}{c_p} \left(\sum_{k=1}^{N_s} c_{p,k} Y_k \mathbf{V}_k \right) \cdot \nabla T \quad (3b)$$

$$C_{Y_k} = -(\mathbf{v} \cdot \nabla) Y_k, \quad D_{Y_k} = -\frac{1}{\rho} \nabla \cdot (\rho Y_k \mathbf{V}_k) \quad (3c)$$

and the source terms by

$$S_T = -\frac{1}{\rho c_p} \sum_{k=1}^{N_s} h_k \dot{\omega}_k, \quad S_{Y_k} = \frac{1}{\rho} \dot{\omega}_k \quad (4)$$

Here, τ is the stress tensor, λ is the mixture thermal conductivity, \mathbf{V}_k is the diffusion velocity of species k , c_p and $c_{p,k}$ are the specific heats at constant pressure for the mixture and species k , respectively, and h_k and $\dot{\omega}_k$ are the specific enthalpy and molar reaction rate, respectively, of species k .

NASA polynomials are used to compute thermodynamic properties. The transport properties are based on a mixture-averaged formulation and are evaluated using the DRFM package [9].

The equation of state (2) is used to derive an expression for the right hand side of the continuity equation (1a)

$$\frac{DP_0}{Dt} = 0 \rightarrow \frac{1}{\rho} \frac{D\rho}{Dt} = -\frac{1}{T} (D_T + S_T) - \sum_{k=1}^{N_s} \frac{\bar{W}}{W_k} (D_{Y_k} + S_{Y_k}) \quad (5)$$

Numerical approach

The numerical integration of the system of equations is performed in three stages. First, a projection approach is adopted to advance the velocity field based on the equations (1a,1b). In the second stage, the scalars are advanced using an operator split approach that separates the convection and diffusion contributions from the ones due to the chemical source terms. Symmetric Strang splitting is employed, beginning with the chemical source term contribution for half the time step, followed by the contributions from convection and diffusion terms for a full time step, and concluded by the remaining contribution from the reaction term for half the time step. The third stage repeats the projection algorithm from the first stage using the updated scalar fields from second stage. Spatial derivatives are approximated using 4th order finite differences.

Stage 1.a

A 2nd-order Adams-Bashforth scheme is used to advance the velocity field using momentum and diffusion terms only

$$\frac{\hat{\mathbf{v}}^{n+1} - \mathbf{v}^n}{\Delta t} = \left(1 + \frac{1}{2} \frac{\Delta t}{\Delta t_o}\right) (C_U^n + D_U^n) - \frac{1}{2} \frac{\Delta t}{\Delta t_o} (C_U^{n-1} + D_U^{n-1}) \quad (6)$$

Superscripts n and $n - 1$ refer to values at the current $t^{(n)}$ and previous $t^{(n-1)}$ times, respectively. The above expression takes into account changes in time step values, $\Delta t = t^{(n+1)} - t^{(n)}$ and $\Delta t_o = t^{(n)} - t^{(n-1)}$.

Stage 1.b

The intermediate velocity field, $\hat{\mathbf{v}}$ does not satisfy the continuity equation (1a). This equation is used in conjunction with the momentum equation (1b) to derive an equation for the hydrodynamic pressure field

$$\nabla \cdot \left(\frac{1}{\rho^{n+1}} \nabla p \right) = \frac{1}{\Delta t} \left(\nabla \cdot \hat{\mathbf{v}}^{n+1} + \frac{1}{\rho} \frac{D\rho}{Dt} \Big|^{n+1} \right) \quad (7)$$

Since the scalar fields at $t^{(n+1)}$ are not yet known, $\frac{1}{\rho} \frac{D\rho}{Dt} \Big|^{n+1}$ is estimated by extrapolation:

$$\frac{1}{\rho} \frac{D\rho}{Dt} \Big|^{n+1} = \left(1 + \frac{\Delta t}{\Delta t_o}\right) \frac{1}{\rho} \frac{D\rho}{Dt} \Big|^n - \frac{\Delta t}{\Delta t_o} \frac{1}{\rho} \frac{D\rho}{Dt} \Big|^{n-1} \quad (8)$$

Fourth-order finite difference discretizations [10] for the variable coefficient Poisson equation (7) lead to consistent linear systems for periodic computational domain. However, for generic configurations the singular linear systems that arise from high-order discretization of eq. (7) are inconsistent. To circumvent this problem we adopt a cell-average formulation for the pressure equation in conjunction with a high-order discretization introduced by Kadioglu *et al* [11]. This formulation is based fourth-order cell-averaged values for ρ , $\nabla \cdot \hat{\mathbf{v}}$, and $\frac{1}{\rho} \frac{D\rho}{Dt}$ computed from their cell-centered counterparts. The solution of the new linear system is the cell-averaged pressure, \tilde{p} . The pressure gradients at the edge centers, required to compute the corrections for the intermediate velocity field, are then extracted from their edge-averaged counterparts by solving band-diagonal systems along each edge of the computational domain.

Stage 1.c

The gradient of the hydrodynamic pressure gradient is used to correct the intermediate velocity field $\hat{\mathbf{v}}^{n+1}$ to obtain the velocity at $n + 1$

$$\mathbf{v}^{n+1,p} = \hat{\mathbf{v}}^{n+1} - \frac{\Delta t}{\rho^{n+1}} \nabla p,$$

where ρ^{n+1} is extrapolated from values at n and $n - 1$ similar to eq. (8). Superscript p was added to \mathbf{v} to distinguish the velocity values obtained at the end of Stage 1 from the ones obtained at the end of Stage 3 below.

Stage 2.a

The stiff integrator package is used to advance scalar fields based on contributions from the source terms, S_T and S_{Y_k} :

$$\begin{aligned} T^* - T^n &= \int_{\Delta t/2} S_T dt \\ Y_k^* - Y_k^n &= \int_{\Delta t/2} S_{Y_k} dt \quad k = 1, 2, \dots, N_s \end{aligned} \quad (9)$$

The time advancement during this stage is done independently for each mesh cell in the grid hierarchy since the RHS (right-hand-side) terms in eq. (9) do not have any spatial dependence. At the end of the stage the scalar values are recursively restricted from the fine to the coarse grid levels in the mesh hierarchy. During this stage, as well as Stages 2.b and 2.c described below density is computed from equation of state (2).

Stage 2.b

A 2nd-order, multi-stage, Runge-Kutta-Chebyshev (RKC) [12] scheme is used to advance scalars based on the contributions from convection and diffusion terms:

$$\begin{aligned} T^{**} - T^* &= \int_{\Delta t} \underbrace{C_T + D_T}_{F_T} dt \\ Y_k^{**} - Y_k^* &= \int_{\Delta t} \underbrace{C_{Y_k} + D_{Y_k}}_{F_{Y_k}} dt \quad k = 1, 2, \dots, N_s \end{aligned} \quad (10)$$

This time integration is performed on all levels of the AMR mesh hierarchy in a “time-refined” manner [3, 13]. A fine-to-coarse restriction on all levels of the mesh hierarchy concludes this stage.

Stage 2.c

Stage 2.c is a repeat of Stage 2.a, using the “**” scalar values as initial conditions

$$\begin{aligned} T^{n+1} - T^{**} &= \int_{\Delta t/2} S_T dt \\ Y_k^{n+1} - Y_k^{**} &= \int_{\Delta t/2} S_{Y_k} dt \quad k = 1, 2, \dots, N_s \end{aligned} \quad (11)$$

At the end of this stage all scalars correspond to t^{n+1} . Similar to Stage 2.a, values are restricted sequentially from fine to coarse grid level to ensure the best available values on all mesh levels.

Stage 3.a

A 2nd order scheme based on both n and $(n + 1)$ values is used to finalize the solution for the velocity field

$$\frac{\hat{\mathbf{v}}^{n+1} - \mathbf{v}^n}{\Delta t} = \frac{1}{2} ((C_U^n + D_U^n) + (C_U^{n+1} + D_U^{n+1})) \quad (12)$$

The convection C_U^{n+1} and diffusion D_U^{n+1} are based on scalar values at t^{n+1} and the velocity field $\mathbf{v}^{n+1,p}$.

Stage 3.b

This stage is similar to Stage 1.b. For this stage $\left. \frac{1}{\rho} \frac{D\rho}{Dt} \right|^{n+1}$ is calculated using the scalar values at t^{n+1} .

Stage 3.c

Stage 3.c is also similar to Stage 1.c. At the end of this stage all the velocity field \mathbf{v}^{n+1} is prolonged sequentially from coarse to fine grid levels.

Adaptive mesh refinement

We employ an block-structured AMR approach where the computational domain is split into rectangular blocks. These blocks are successively refined in the regions where the current grid resolution is not sufficient to capture the physics of interest. These blocks comprise a grid hierarchy where blocks on a given level are completely embedded in blocks on the immediately coarser level. A coarsening algorithm is also employed to remove computational blocks where higher grid density is no longer necessary.

The advancement in time of the AMR solution is based on Berger-Colella time refinement [3, 13]. Figure 1 shows a schematic of the recursive time integration. Consider the solutions on levels L and $L + 1$ at time t_n . Level L is first advanced to $t_n + \Delta t$, then the solution on $L + 1$ is advanced in two half steps, $\Delta t/2$ to ensure the scheme stability on the finer grid. During time advancement on $L + 1$, boundary conditions are computed by interpolation using the solution on L . At $t_n + \Delta t$ the solution on $L + 1$ is interpolated down to the corresponding regions on level L . In order to preserve the 4th-order spatial convergence of the numerical scheme, the interpolations between adjacent grid levels use 6th-order spatial stencils [14].

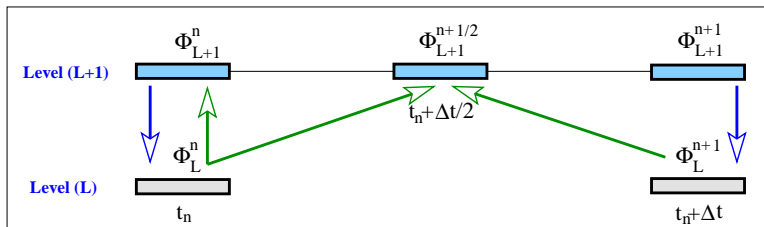


Figure 1: Schematic of the time refinement in the context of AMR.

Δt range [s]	T	ρ	u	∇p	Y_{CH_4}	Y_{CO_2}	Y_{CH_3}	Y_{HCO}
$(50 \rightarrow 25 \rightarrow 12.5) \times 10^{-8}$	1.92	1.92	1.97	1.58	1.92	1.85	1.94	1.53
$(25 \rightarrow 12.5 \rightarrow 6.25) \times 10^{-8}$	2.01	2.01	2.02	1.84	2.00	1.97	2.00	1.48
$(12.5 \rightarrow 6.25 \rightarrow 3.125) \times 10^{-8}$	2.07	2.07	2.07	1.96	2.05	2.05	2.05	1.84
$(6.25 \rightarrow 3.125 \rightarrow 1.5625) \times 10^{-8}$	2.17	2.18	2.17	2.01	2.13	2.16	2.12	1.94

Table 1: C1-mechanism convergence rates for 1D simulations using 3 mesh levels. The grid size on the coarse mesh level is $\Delta_x = 30\mu m$. Solutions are advanced for $t = 0.4ms$ and errors are measured in a region $1.2T_{min} < T < 0.8T_{max}$.

Results

Both one-dimensional (1D) and two-dimensional (2D)) configurations are used to test the numerical scheme presented in the previous section. Due to their computational expense, time convergence rates are measured only in 1D configurations, while spatial convergence rates are measured both in 1D and 2D configurations. All tests involve methane combustion, and chemistry is modeled using a C₁ skeletal mechanisms with 16 species and 46 reversible reactions [15].

Time Convergence

For time convergence tests, the initial condition corresponds to a freely propagating premixed flame, computed with Chemkin’s Premix package [16]. The computational domain is 1.5 cm. A premixed flame propagates from right to left into an unburnt stoichiometric methane-air mixture. The initial solutions from the Chemkin package were relaxed on successively refined grids to ensure consistent initial conditions for the convergence tests. Figure 2 shows sample major species and radicals mass fractions profiles for a freely propagating premixed flame used to for the multi-level convergence test. Table 1 shows select results for time convergence tests using a 3-level mesh. All variables exhibit 2nd-order time convergence.

Spatial Convergence

The spatial convergence rates were first first computed using the same configuration as for the time convergence tests shown in the previous section. For this series of tests the Chemkin

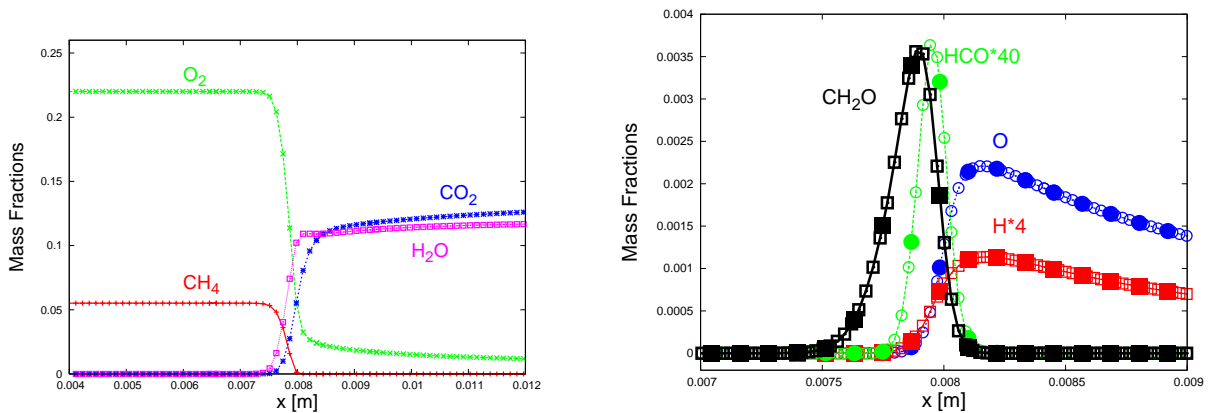


Figure 2: Sample major species (left) and radicals (right) mass fraction profiles for a freely propagating stoichiometric CH_4 -air flame. In the right figure, the filled symbols correspond to the coarse mesh level (1) and the open symbols to the finest mesh level (3).

Δx range [μm]	T	ρ	u	∇p	Y_{CH_4}	Y_{CO_2}	Y_{CH_3}	Y_{HCO}
30 \rightarrow 15 \rightarrow 7.5	3.9	4.0	3.9	3.8	3.9	3.8	3.6	3.9
15 \rightarrow 7.5 \rightarrow 3.75	3.9	3.9	3.9	3.6	4.0	3.6	3.5	3.6

Table 2: C1-mechanism convergence rates for 1D simulations using 3 mesh levels. Solutions are advanced with a time step $\Delta_t = 10^{-8}$ for $t = 0.2\text{ms}$. The grid sizes in the left column correspond to the coarse mesh level. Errors are measured in a region $1.2T_{\min} < T < 0.8T_{\max}$.

solution is first relaxed on the mesh with the finest grid size. The initial conditions for the coarser computational grid are then obtained by interpolation using a 6th-order stencil. The results presented in Table 2 show 4-th order spatial convergence for all variables.

Flame-Vortex Interaction

A canonical vortex-flame configuration [2] was chosen to explore the performance of the numerical construction. The computational domain is $(1.5 \times 0.75) \times 10^{-2}$ m in the streamwise and transversal directions, respectively. The velocity field corresponding to a periodic row of counter-rotating Lamb-Oseen vortices is superimposed over the premixed 1D flame solution discussed above. A relatively coarse mesh was used for the base mesh, with a cell size of $58\mu\text{m}$ in each direction. Additional, finer, mesh levels were added in the flame region during the simulation.

A one-step, irreversible Arrhenius global reaction model is used in addition to the C1 kinetic model to study the vortex-flame interaction. Figures 3 and 4 show freeze frames of the vorticity and heat release rate fields. The vortex pair is initially located 2×10^{-3} m upstream of the flame and propagates with approximately 10m/s towards it. As the vortex pair impinges into the flame, the flame intensity decreases on the centerline for the C1

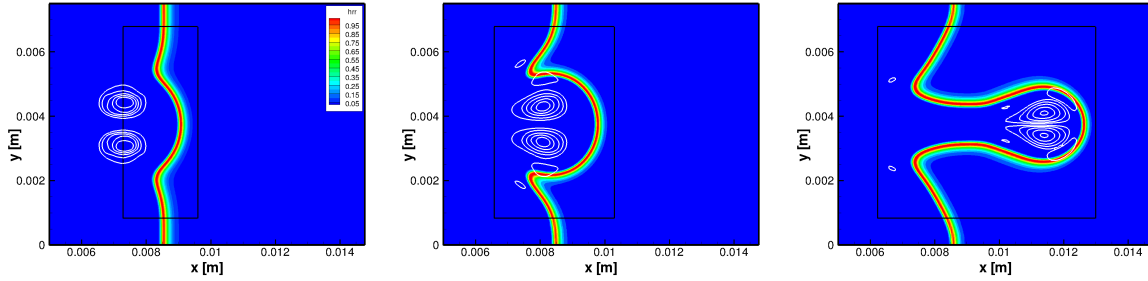


Figure 3: Vorticity (white solid contours) and normalized heat release rate (hrr, shaded contours) for a simulation using the one-step reaction model.

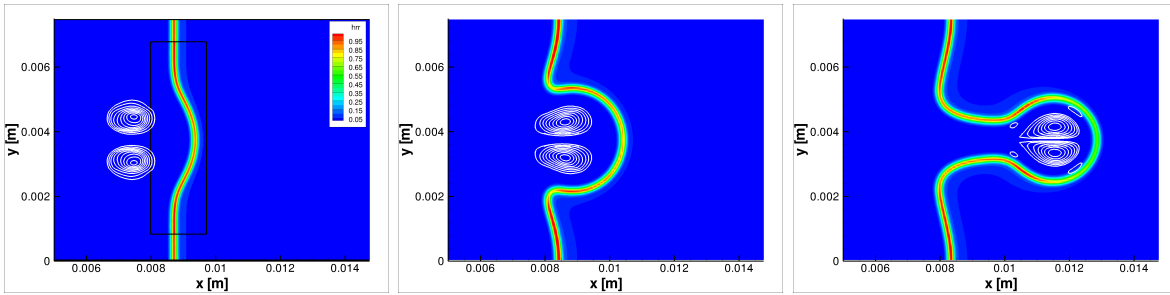


Figure 4: Vorticity (white solid contours) and normalized heat release rate (hrr, shaded contours) for a simulation using the C1 kinetic model.

model while the one-step solution shows little change in the interaction region. Similarly, at locations off-centerline the flame intensity for the C1 model decreases significantly as it stretched and rolled around the vortex pair. The last frames show a significantly contorted flame, and the relative increase in the overall burning rate is about about 50% more for the one-step reaction simulation compared to the simulation using the C1 model .

The AMR procedure allows to one to overlay a finer computational mesh in the region where the flame interacts with the vortex pair while maintaining a coarse resolution elsewhere. In Figure 5, we show mass fraction profiles for select radicals along the centerline during the interaction. The AMR mesh has 2 levels, with a factor of 2 refinement between the coarse and fine levels. The results from the two levels are indicated by c and f as subscripts in Fig. 5. While the finer mesh level is not necessary for the “slow” OH radical, its benefits are evident for the narrow HCO mass fraction profile.

Summary and Conclusions

This paper introduces a new high-order numerical model for the study of chemically reacting flow in the low-Mach number limit. A 4-th order (in space) projection algorithm for the momentum transport is coupled with an adaptive mesh refinement procedure of the same order for the transport of energy and species mass fractions. Canonical 1D and 2D configurations are used to investigate the performance of the numerical construction. Future work

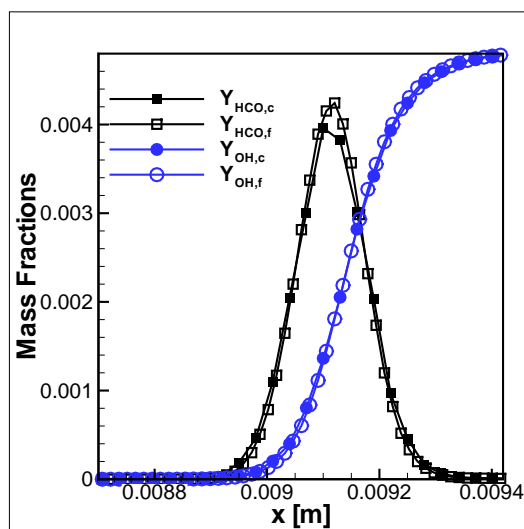


Figure 5: *HCO* and *OH* mass fraction profiles on the centerline during the flame-vortex interaction, simulated on a 2-level AMR mesh. Results obtained on the coarse mesh are indicated by *c* in the subscript; the fine-resolution results are indicated by *f*.

will focus on investigating the efficiency of this methodology using detailed kinetic models in the context of laboratory scale flame configurations.

Acknowledgments

This work was supported by the US Department of Energy (DOE), Office of Basic Energy Sciences (BES), SciDAC Computational Chemistry program. Sandia National Laboratories is a multiprogram laboratory operated by Sandia Corporation, a Lockheed Martin Company, for the United States Department of Energy under contract DE-AC04-94-AL85000.

References

- [1] Majda, A., and Sethian, J., *Comb. Sci. and Technology*, 42:185–205 (1985).
- [2] Najm, H.N., and Knio, O.M., *J. Sci. Comp.*, 25(1):263–287 (2005).
- [3] Berger, M.J., and Colella, P., *J. Comput. Phys.*, 82:64–84 (1989).
- [4] Bennett, B.A.V., and Smooke, M.D., *Combust. Theor. Model.*, 2(3):221–258 (1998).
- [5] Ray, J., Najm, H.N., Milne, R.B., Devine, K.D., and Kempa, S., *Proc. Combust. Inst.*, 28:219–226 (2000) Part 1.
- [6] Day, M.S., and Bell, J.B., *Combust. Theor. Model.*, 4(4):535–556 (2000).

- [7] Anthonissen, M.J.H., Bennett, B.A.V., and Smooke, M.D., *Combust. Theor. Model.*, 9(2):273–299 (2005).
- [8] Martin, D.F., and Colella, P., *J. Comp. Phys.*, 163:271–312 (2000).
- [9] Paul, Phillip H., Sandia Report SAND98-8203, Sandia National Laboratories, Albuquerque, New Mexico, (1997).
- [10] F, Nicoud, *J. Comput. Phys.*, 158(1):71–97 (2000).
- [11] Kadioglu, S.Y., Klein, R., and Minion, M.L., *J. Comp. Phys.*, 227:2012–2043 (2008).
- [12] Verwer, J. G., Sommeijer, B.P., and Hundsdorfer, W., *J. Comput. Phys.*, 201(1):61–79 (2004).
- [13] Lefantzi, S, Ray, J, Kennedy, CA, and Najm, HN, *Prog. Comput. Fluid Dyn.*, 5(6):298–315 (2005).
- [14] Ray, J., Kennedy, C.A., Lefantzi, S., and Najm, H.N., *SIAM J. Sci. Comp.*, 29(1):139–181 (2007).
- [15] Smooke, M.D., and Giovangigli, V., *Reduced kinetic mechanisms and asymptotic approximations for methane-air flames*, volume 384 of *Lecture Notes in Physics* chapter 1 Springer-Verlag, Berlin, (1991).
- [16] Kee, R.J., Grcar, J.F., Smooke, M.D., and Miller, J.A., Sandia Report SAND85-8240, Sandia National Labs., Livermore, CA, (1993).